Lab on a Chip

Devices and applications at the micro- and nanoscale

Accepted Manuscript

This article can be cited before page numbers have been issued, to do this please use: T. Xu, Y. J. Lim, Y. zheng, M. S. Jung, K. Gaus, E. Gardiner and S. Lee, *Lab Chip*, 2020, DOI: 10.1039/D0LC00598C.

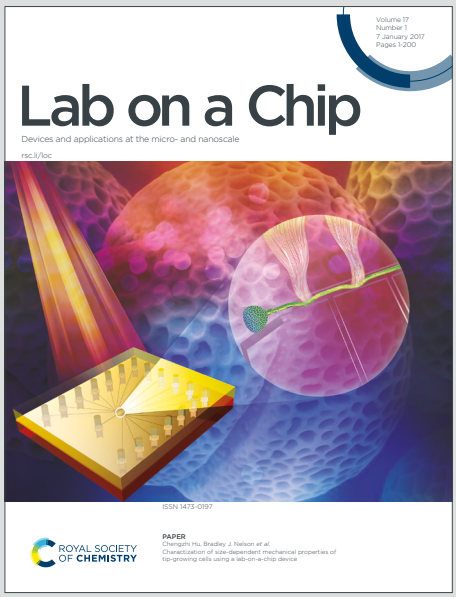

ROYAL SOCIETY OF CHEMISTRY

rsc.li/loc

View Article Online
DOI: 10.1039/D0LC00598C

ARTICLE

Modified inverted selective plane illumination microscopy for sub-micrometer imaging resolution in polydimethylsiloxane soft lithography devices

Received 00th January 20xx,
Accepted 00th January 20xx

DOI: 10.1039/x0xx00000x

Tienan Xu,[a] Yean Jin Lim,[a, b] Yujie Zheng,[a] Moon Sun Jung,[c] Katharina Gaus,[c] Elizabeth E. Gardiner [b] and Woei Ming Lee [a, b, d]

Moldable, transparent polydimethylsiloxane (PDMS) elastomer microdevices enable a broad range of complex studies of three-dimensional cellular networks in their microenvironment in vitro. However, the uneven distribution of refractive index change; external to PDMS devices and internally in the sample chamber, create significant optical path difference (OPD) that distorts the light sheet beam and so restricts diffraction limited performance. We experimentally showed that an OPD of 120 µm results in the broadening of the lateral point spread function by over 4 folds. In this paper, we demonstrate steps to adapt an commercial inverted Selective Illumination Plane Microscope (iSPIM) and remove OPD so as to achieve sub-micrometer imaging ranging of 0.6±0.04 µm to 0.91±0.03 µm of fluoresence biological sample suspended in regular saline (RI≈1.34) enclosed in 1.2 to 2 mm thick micro-molded PDMS microdevices. We have proven that the removal of OPD from external PDMS layer by refractive index (RI) matching with readily accessible, inexpensive sucrose solution is critical to achieve a >3 fold imaging resolution improvement. To monitor the RI matching process, a single mode fiber (SMF) illuminator was integrated into the iSPIM. To remove the OPD inside the PDMS channel, we used an electrically tunable lens (ETL) that par-focus the light sheet beam with the detection objective lens and so minimised axial distortions to attain sub-micrometer imaging resolution. We termed this new light sheet imaging protocol as modified inverted Selective Plane Illumination Microscopy (m-iSPIM). Using the high spatial-temporal 3D imaging of m-iSPIM, we experimentally captured single platelet (≈2 µm) recruitment to a platelet aggregate (22.5 µm x 22.5µm x 6 µm) under flow at a 150 µm depth within a microfludic channel. m-iSPIM paves the way for the application of lightsheet imaging to a wide range of 3D biological models in microfluidc devices which recapitulate features of the physiological microenvironment and eludicate sub-cellular responses.

Introduction

Polydimethylsiloxane (PDMS) plays a ubiquitous role in soft lithography[1] because of its ability to facilitate rapid and consistent prototyping of arbitrarily shaped three-dimensional (3D) microfluidic chambers in geometries that recapitulate cellular microenvironments.[2] PDMS elastomeric structures possess a unique combination of biochemical compatibility, optical transparency and mechanical properties that makes it a suitable material for microfluidic devices to achieve microenvironment control of complex 3D cell culture and imaging using high-resolution fluorescence microscopy.[3] Although the synergy between high speed volumetric fluorescence microscopy imaging and transparent microfluidics devices allows controlled four dimensional (space and time) quantification of various complex biological models, point scanning volumetric imaging performance is hindered by phototoxicity and photobleaching due to high illumination power.[3] On the other hand, light sheet fluorescence microscopy (LSFM) conducts rapid volumetric imaging with low phototoxicity[4-6] because the illumination power densities are at least two orders of magnitude lower than conventional confocal microscopes.[7]

Combining standard LSFM with conventional PDMS microfabricated devices faces a major problem of optical distortion.[8] Focused beams in LSFM can experience significant optical path difference (OPD) across interfaces that reduces the imaging resolution.[9] OPD is defined by refractive index (RI) difference (Δn) multiplied by light propagation distance (d). In most PDMS microdevices, the propagation distance of light through a layer of PDMS material is generally an order of magnitude longer (10^3 µm) than the internal sample space (10-10^2 µm).[10] Hence, a thick PDMS layer is likely to constitute the majority of the total OPD in microdevices. This is illustrated in Fig. 1a i), where the excitation (blue) and emission (green) beams are distorted by a thick PDMS layer before reaching the

[a] Research School of Electrical, Energy and Materials Engineering, College of Engineering and Computer Science, The Australian National University, Canberra, ACT 2601, Australia
[b] ACRF Department of Cancer Biology and Therapeutics, The John Curtin School of Medical Research, The Australian National University, Canberra, ACT 2601, Australia
[c] EMBL Australia Node in Single Molecule Science and ARC Centre of Excellence in Advanced Molecular Imaging, The University of New South Wales, Sydney, NSW 2052, Australia
[d] ARC Centre of Excellence in Advanced Molecular Imaging, The Australian National University, Canberra, ACT 2601, Australia
Electronic Supplementary Information (ESI) available. See DOI: 10.1039/x0xx00000x

View Article Online
DOI: 10.1039/D0LC00598C

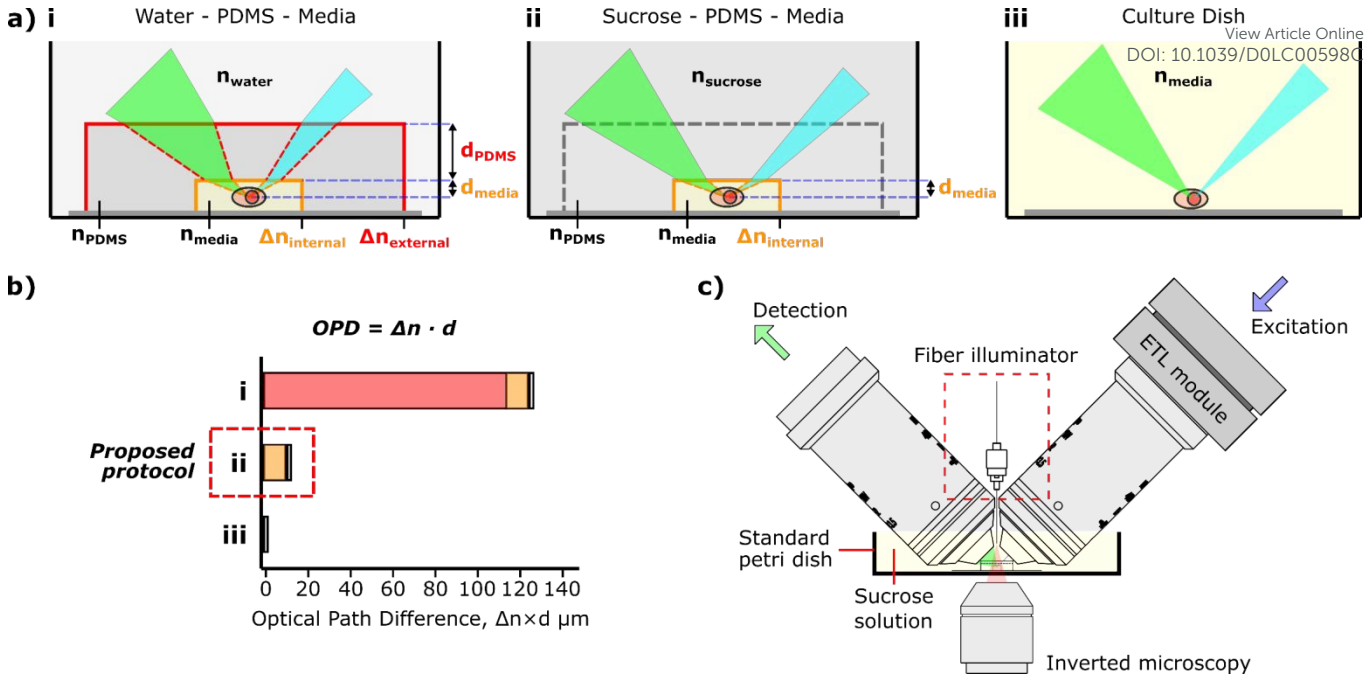

Fig. 1 a) Diagram of iSPIM imaging through a PDMS device with i) water or ii) RI-matched sucrose solution as the objective lens immersion medium. Refractive index mismatch from external (red, $\Delta n_{external}$) and/or internal (orange, $\Delta n_{internal}$) interfaces results in distorted beam paths through the PDMS and internal media with depth of d_{PDMS} and d_{media}, respectively. iii) Diagram of ideal iSPIM imaging without PDMS device where both objective lenses and samples are immersed in media. b) Optical path difference (OPD) induced by RI-mismatch (Δn) and propagation depth (d) of the three imaging scenarios in a). For completeness, a slight portion of OPD incurred at the sample-media interface is included for all three scenarios. c) Illustration of the m-iSPIM with an ETL module and a fiber illuminator.

sample of interest in an inverted Selective Plane Illumination Microscopy (iSPIM) system.[11] Here, the external water-PDMS interface ($\Delta n_{external}$) and the internal PDMS-media interface ($\Delta n_{internal}$) both contribute to the total OPD (Fig. 1b). Fig. 1a ii) shows that if $\Delta n_{external}$ is eliminated using a water-sucrose solution, i.e. RI matched to PDMS, the overall OPD and hence, optical distortion, is significantly reduced to match closer to the ideal imaging scenario (e.g. without PDMS interfaces, Fig. 1a iii).

Fig. 1b) shows an estimate of the OPD for the three different scenarios illustrated in Fig. 1a). Estimations for Δn and propagation distance are based on a PDMS chip design, where a single 100 μm-deep microchannel (d_{media}) is filled with RI=1.34 media (n_{media}) that is enclosed in PDMS layer 1000 μm in thickness (d_{PDMS}) and with a of RI=1.41. Thus, we calculated an OPD of approximately 130 μm when a water-PDMS external interface is present, despite a small $\Delta n_{external}$ of 0.08. By eliminating $\Delta n_{external}$ using a sucrose solution ($n_{sucrose}$ =1.41), the OPD can be reduced by approximately 8-fold. Remaining OPD incurs minor axial focal shifts in both the excitation and emission beams (i.e. longer parfocal distance) because conventional LSFM objective lenses are corrected for water.[11]

Existing LSFM microfluidic imaging solutions overcome the OPD by involving (1) the use of specialized LSFM-compatible PDMS microdevices and PDMS-like material,[12-21] (2) re-engineering the excitation and detection paths with single-objective LSFM[22-24] or (3) imaging from beneath the coverslip instead of PDMS.[25-29] Drawbacks of approach (1) include extensive PDMS microfabrication procedures or use of moldable materials with lower elasticity or permeability to gases. The approach (2) requires extensive re-designing of the scanning and imaging paths due to oblique angles. Such modification to the optical setup can reduce potential access to other essential tools used in microfluidic studies such as optical micromanipulation[30] and widefield quantitative imaging.[31] Approach (3) leverages specialized immersion chambers with a solid immersion meniscus lens as well as a clearing protocol that is generally more accessible using lower numerical aperture (NA) objective lenses (≈0.7).

In order to test our OPD hypothesis (matching $\Delta n_{external}$ only), adhering to existing soft lithography PDMS microdevices as well as carrying out minimal modification to the existing LSFM system, we propose a modified iSPIM (m-iSPIM) imaging approach. The proposed m-iSPIM approach requires two additional components: an electrically tunable lens (ETL) module and a fiber illuminator incorporated into a standard iSPIM system.[11] The ETL module compensates for the excitation beam's axial focal shift and a fiber illuminator provides an additional light source to facilitate elimination of $\Delta n_{external}$. These modest alterations can also be adaptable for a diSPIM,[32] reflective diSPIM system[33] and possibly lattice light sheet microscopy (LLSM),[34] which require objective lenses of 1.1 NA and around 2 mm working distance. To prove that the m-iSPIM can deliver sub-micrometer imaging performance through PDMS microdevices with millimeter thickness, we performed a series of validation experiments using sub-diffraction limited (100 nm) beads, live L929 fibroblast cells, fixed spheroids and flowing live human platelets using microfabricated PDMS microdevices. Our solution aims to accommodate for the growing needs of biological imaging users that will employ PDMS microfluidic devices for studies using organs on a chip[35] biological fluidic imaging and 3D organoid cultures.[13, 36]

View Article Online
DOI: 10.1039/D0LC00598C

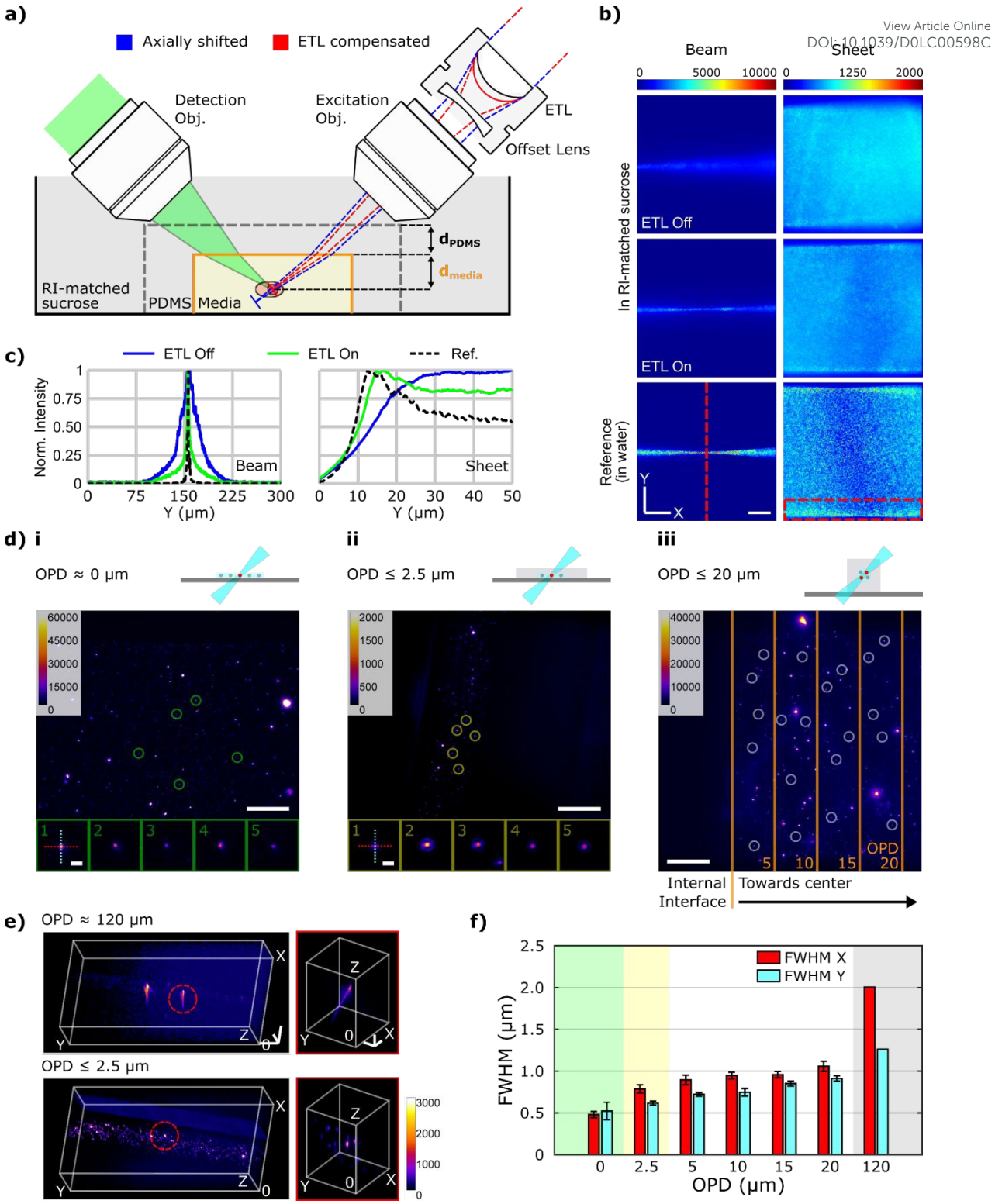

Fig. 2 a) Illustration showing ETL axial focus tuning of the excitation beam. The axially shifted beam is shown in blue while the compensated beam is shown in red. b) Images of the excitation beam and scanned light sheet revealed by fluorescent highlighter solution mixed in the objective immersion medium. Dashed lines indicate the selection for the line profile in c). Scale bar: 50 μm. c) (left) Normalized intensity profile of the excitation beam at the center of the imaging FOV and (right) of the light sheet at its edge. d) Imaging of 100 nm beads i. fixed on a coverslip, ii. embedded in a PDMS microchannel or iii. embedded in a PDMS microchamber, where i) water (OPD≈0 μm) or ii) and iii) RI-matched sucrose solution (OPD≤2.5 or 20 μm) was used as the objective immersion medium. Orange lines in iii) are 5 μm OPD intervals (corresponds to 50 μm depth intervals) starting from the internal interface. Insets show magnified images of selected bead with dashed lines indicating lines for determining X (red) and Y (cyan) FWHM. Scale bar: 50 μm and 10 μm (insets). e) Volumetric reconstruction of 100 nm beads embedded in PDMS microchannel with OPD≈120 μm (top) or OPD≤2.5 μm (bottom). Scale bar: 30 μm (left), 10 μm (right). f) Bar plot of the FWHM in X and Y direction quantified from d) and e).

Method

To validate imaging performance of the m-iSPIM, four different types of PDMS microdevices of varying thickness, geometries and dimensions were fabricated using micromolding (Supplementary Fig. 1 to 4). Briefly, a degassed PDMS mixture (1:10, curing agent to base volumetric ratio, v/v, Slygard 184, Dow Corning) is poured onto the designed mold and cured at 80°C for 2 hours. The cured PDMS block is cut with inlets/outlets made where necessary, then bonded to a coverslip after surface plasma treatment. Sucrose solution is prepared by dissolving solid sucrose powder (AJA530-500G, Ajax Finechem) in water at a concentration of 50% (w/v). This corresponds to a RI of 1.420, as determined by a refractometer (HI96800, Hanna Instruments) then was diluted to match PDMS, which varies from RI = 1.410 to 1.414.

Samples for static imaging were prepared by either fixation, embedding or suspension in saline within the PDMS microdevices. Quantitative assessments of imaging resolution are performed using sub-diffraction limited (100 nm) fluorescent beads (ex505/em515, F8803, Invitrogen) embedded in agarose solution (RI=1.3358, 4% w/w agarose-PBS) at a 1:50 (v/v) dilution. For live cell imaging, L929 fibroblasts were trypsinized, washed in PBS and stained with Vybrant DiO dye (1:200 dilution (v/v), Invitrogen) for 15 minutes prior to further washing and resuspension in PBS. Spheroids were generated from a 5-day culture of the MCF-7 cancer cell line stained with the membrane-specific dye DiO and seeded at 2500 cells/well in an ultra-low attachment, round bottom 96-well plate (CLS7007, Corning Costar), then fixed with 4% paraformaldehyde, prior to staining with phalloidin conjugated to Alexa Fluor 568. After washing with PBS, bound fluorescence revealed contours of the cell membrane as well as non-specific binding of phalloidin to interstitial matrix between cells.

Monitoring of platelet aggregation was used to validate the spatial-temporal imaging capability of the m-iSPIM within PDMS microdevices.[37] Washed platelets were prepared from anticoagulated venous whole blood collected from healthy donors after provision of informed consent (project approval granted by the Australian National University Human Research Ethics Committee, 2016/317). Blood was collected into acid-citrate-dextrose solution (1.25 g trisodium citrate, 1.0 g glucose, 0.75 g citric acid, per 50 mL distilled water) and centrifuged at 110 *g* for 20 minutes with no brake. The upper phase containing platelets were then isolated by centrifugation (1271 *g* for 15 minutes with high brake). The platelet pellet was resuspended three times in citrate-glucose-saline buffer (1.44 g NaCl, 1.2 g glucose, 0.76 g trisodium citrate, per 200 mL distilled water, pH 7.0) and centrifuged (1271 *g* for 15 minutes) then finally resuspended in Tyrode's buffer (4 g NaCl, 1 g $NaHCO_3$, 1 g glucose, 0.2 g KCl, 0.2 g $CaCl_2$, 0.1 g $MgCl_2$, 0.05 g NaH_2PO_4, per 500 mL distilled water, pH 7.4) to reach a final platelet count of 1×10^8 platelets/mL. All centrifugations were conducted at room temperature. Platelets were incubated with 10 mM $DiOC_6$ intracellular lipophilic dye (in DMSO stock, Invitrogen D273) for 30 minutes. To generate flow, a PDMS microdevice outlet was connected to a syringe housed within a syringe pump (PHD2000, Harvard Apparatus) in suction mode using a customized infusion connection (Supplementary Fig. 4). The device channel was filled with collagen (Type-I, 100 µg/mL, Takeda, Austria) and incubated at 4°C for 18 hours. Prior to the experiment, the channel was flushed with Tyrode's buffer at 200 µL/min for 2 minutes. For the experiment, the suspension of washed platelets was placed in a reservoir and drawn into the PDMS channel under negative pressure, at a volume rate of 10 µL/min which is equivalent to a wall shear rate of 7.86 s^{-1}.

Results

Construction of the m-iSPIM

The basic iSPIM setup generates a light sheet from a laser beam (488 nm, 06-MLD, Cobolt) scanned by a MEMS-mirror scanner (MM-SCAN_1M, ASI) and relayed to the excitation objective lens fixed on a manual rotating mount 45° above the sample space. The detection objective lens is mounted on the same rotating mount and a piezoelectric Z-translation mount (150 µm, PZMAG-RAO-M25, ASI). Depth (Z) scanning through the sample is achieved by co-alignment and synchronizing the scanning light sheet with the axial position of detection objective lens image plane through the sample.[11] Each Z-slice is recorded by a scientific complementary metal-oxide-semiconductor (sCMOS) camera (pco.edge 4.2, PCO). Hardware and software control of the iSPIM system is managed by Micro-Manager.[38]

The modification of iSPIM to create the m-iSPIM is shown in Fig. 1c. Firstly, an optical fiber is mounted between the pair of orthogonally mounted iSPIM objective lenses (40X, 0.8 NA, 3.5 mm WD, N40X-NIR, Nikon) to create an independent illumination that is projected into the sample space. The width of the single mode fiber (SMF, 125 µm dia.) fits within the tight gap (≈700 µm width) between the two objective lenses of the iSPIM and its NA (≈0.13) allows transmitted light to be collected by an objective lens (10X, 0.3 NA, 10 mm WD, RMS10X-PF, Olympus). In the m-iSPIM, the transmitted light is relayed and combined with the reference light from the other fiber through a tilted 50:50 beam splitter (CCM1-BS013, Thorlabs), to form an interference pattern at a charge coupled device (CCD) camera (pco.pixelfly USB, PCO). The interference pattern allows us to measure the OPD within the sample i.e. off-axis quantitative phase microscopy (QPM).[39] Alternatively, one can also use in-line defocusing-based methods to conduct quantitative phase measurements albeit with additional computing steps.[40]

Secondly, an ETL module,[41] a convex tunable lens (EL-10-30-C-VIS-LD, Optotune) paired with a plano-concave offset lens (f=-48 mm, #45-018, Edmund Optics), is mounted to the back of the iSPIM's excitation objective lens. The module replaces the manual rotating mount and is shown in detail in Fig. 2a. This assembly is then fixed on the iSPIM frame using commercially available optomechanical parts (Thorlabs Inc). A USB driver (Lens Driver 4, Optotune) digitally controls the current delivered to the ETL for fine-tuning the axial focus without physically shifting the objective lens. As with any light sheet imaging, it is necessary to manually center the light sheet to the iSPIM

detection objective lens field of view (FOV). Visualization of m-iSPIM images is performed in Fiji.[42] We conducted post-processing steps to improve image contrast and remove out of focus fluorescence light depending on the sparsity of the biological samples using Fiji and LsDeconv[43]. Both background subtraction and deconvolution were performed for densely packed spheroid images, while deconvolution was applied for sparsely distributed platelet and fibroblast cell images. All in all, the m-iSPIM requires minimal changes to existing iSPIM operation and can support an RI of up to ≈1.42 (sucrose solution ≈50% concentration), which is adequate to match the RI of conventional PDMS microdevices.[44]

Measuring beam waist of m-iSPIM's light sheet

Since different batches of PDMS can exhibit slight variations in RI, and hence OPD, we developed a method to monitor changes of OPD over time. For this, we employed QPM to measure the difference between the phase of light transmitted through the PDMS and sucrose solution, which is associated with $\Delta n_{external}$ (Supplementary Fig. 5). The monitoring of $\Delta n_{external}$ and live adjustments of the sucrose concentration ensures that there is minimal OPD, i.e. $\Delta n_{external}$ is close to zero. We then record the RI of the sucrose solution using a refractometer. The RI measurement is accurate for all PDMS devices of the same batch. Subsequent OPD measurement is only required at the start of each experiment to ensure RI-matched condition between PDMS and sucrose solution.

The width of the light sheet beam is a direct measure of the optical sectioning ability in light sheet imaging.[45] Hence, it is necessary to quantify the intensity profile of the light sheet beam using a fluorescence dye. Fig. 2b) shows that the use of sucrose solution matched to the RI of PDMS (≈1.41) and paired with an objective lens corrected for the RI of water (1.33) induces significant axial focal shift of ≈300 µm in the excitation beam and sheet. By setting the ETL current to 180 mA, the light sheet is focused back to the center of the FOV of the detection objective lens. Additional adjustment of axial focal shift in the detection path can be achieved with manual adjustments to the objective lens mount. The excitation light beam and sheet without any optical distortion is shown alongside for comparison. The improvement of the intensity profile becomes more evident by comparing the intensity plot of the beam waist and the intensity gradient at the edge of light sheet as shown in Fig. 2c). By engaging the ETL, the excitation beam is sharpened considerably and results in approximately 8.12-fold reduction of the full width half maximum (FWHM) from 30.45 µm to 3.75 µm. The improvement is also observed in the intensity gradient ≈40 µm from edge of the light sheet (Fig. 2c), which indicates an increase in intensity gradient ($\Delta I_{normalized}$) from 0.005 μm^{-1} to 0.01 μm^{-1}.

Quantifying sub-micrometer imaging resolution in PDMS devices

To further validate our method, we investigated the imaging resolution achievable in PDMS microdevices of different

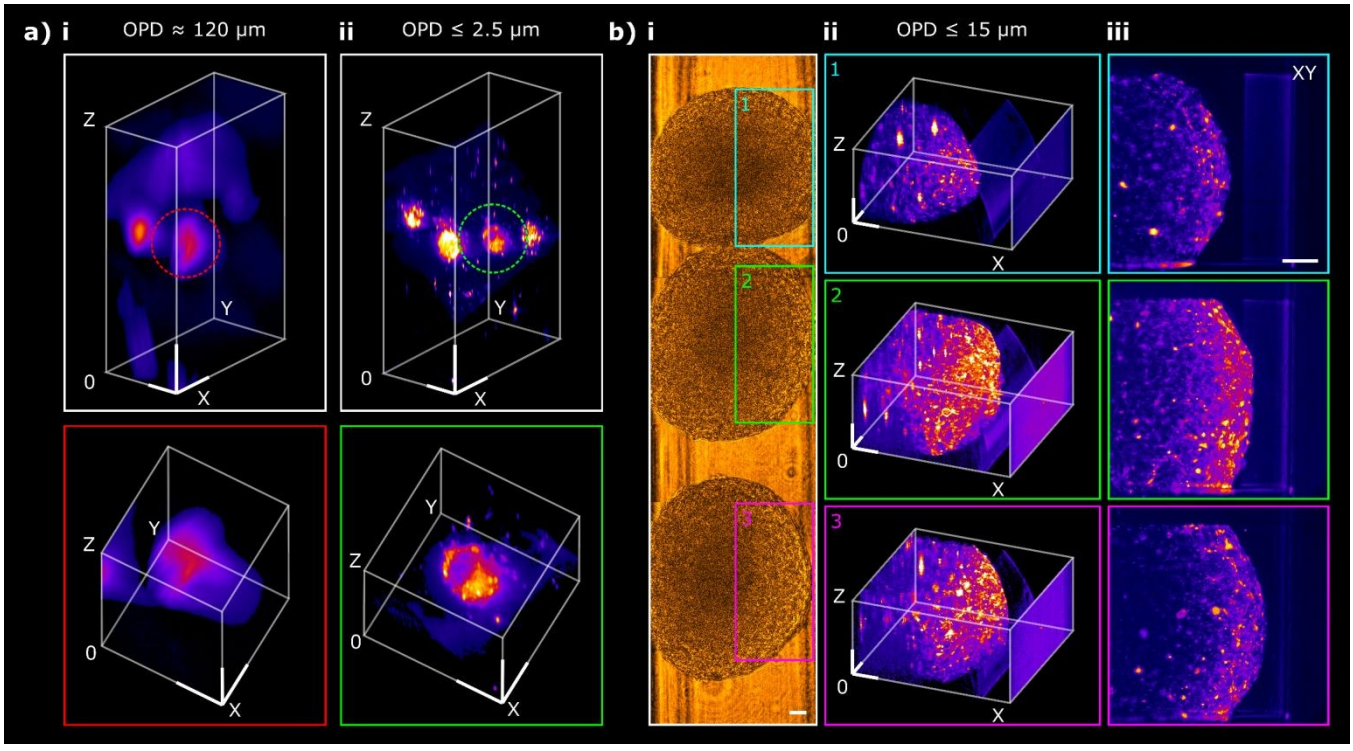

Fig. 3 a) Volumetric reconstructions of live, DiO-stained fibroblast cells in a microchamber device and imaged with an OPD of i) ≈120 µm or ii) ≤2.5 µm. Scale bar: 30 µm. Insets show zoomed-in views of selected cells. Scale bar: 20 µm. b) i) Reconstructed brightfield images obtained by inverted QPM showing fixed L929 spheroids stained with Vybrant DiO and Alexa Fluor 568-Phalloidin, lined up in a microchamber device and imaged with $\Delta n_{external}$=0 (OPD≤120 µm). Scale bar: 50 µm. ii) Volumetric reconstructions of m-iSPIM imaging of corresponding spheroid regions highlighted in i (color-coded). Scale bar: 50 µm. iii) XY slice of the spheroid. Scale bar: 50 µm. All volumetric reconstructions were generated using Fiji Volume Viewer with maximum intensity projections and trilinear interpolation. List of RI: water – 1.332; gelatin – 1.340; PBS – 1.340; microchannel – 1.4120; chamber – 1.4117; microchamber – 1.4134. Sucrose solution matches the RI of PDMS device used.

View Article Online DOI: 10.1039/D0LC00598C

thickness. For this we imaged sub-diffraction limited fluorescent beads fixed on a coverslip i.e. d_{PDMS}=0 µm or flowed into PDMS microdevices of different thickness d_{PDMS}=1200 µm and 2000 µm (Fig. 2 d-f). Fig. 2d i) indicates that without any PDMS, i.e., OPD≈0 µm, the ETL-refocused light sheet in the m-iSPIM retrieves a lateral resolution of 0.48±0.04 µm (FWHM X) and 0.52±0.11 µm (FWHM Y) that is comparable with diffraction limited results from iSPIM.[11] The lateral resolution becomes to X=0.79±0.05 µm and Y=0.62±0.02 µm in a 1200 µm-thick PDMS chamber at a sample depth (d_{media}) of 25 µm, where OPD is less than 2.5 µm (Fig. 2d, ii). For a PDMS chamber with a thickness of 2000 µm (Fig. 2d, iii), the lateral imaging resolution varies from X=0.89±0.06 µm, Y=0.72±0.02 µm at d_{media} of 50 µm to X=1.06±0.06 µm, Y=0.91±0.03 µm at d_{media} of 200 µm, covering OPD ranging from 0 to 20 µm. In contrast, beads in PDMS chamber imaged without eliminating $\Delta n_{external}$ showed significant optical aberration (Fig. 2e) that degraded the achievable lateral resolution to X=2.01 µm and Y=1.26 µm. Fig. 2f) summarizes the point spread function (PSF) measurements from Fig. 2d and 2e, which clearly demonstrates the greater impact of changing $\Delta n_{external}$ from 0 (sucrose-PDMS) to 0.08 (water-PDMS) on lateral resolution against increasing d_{media}. We note that the consistent asymmetry of the PSF in the X- and Y-direction (≈21±7%) is likely a result of laser polarization. These results validate our hypothesis that the m-iSPIM approach removes the majority of the OPD from PDMS microdevices to achieve sub-micrometer resolution ideal for cellular imaging. Thus, we next moved to verify the m-iSPIM for imaging biological samples within PDMS devices.

Imaging biological samples

LSFM has been implemented for studies at the microscopic (e.g. single cell and intracellular) and macroscopic (e.g. spheroid and embryo) level[7] and as such, we aimed to demonstrate that the m-iSPIM can encompass both scales of imaging. For this we imaged L929 fibroblast cells and fixed tumor spheroids suspended in saline (n_{media}≈1.34) within PDMS chambers (Fig. 3). Fig. 3a) presents 3D volumetric images of L929 fibroblast cells stained with Vybrant DiO dye in a PDMS microdevice using either standard iSPIM or the m-iSPIM. Our results clearly show that the removal of $\Delta n_{external}$ and the refocusing by the ETL in the m-iSPIM achieves finer intracellular details as apparent in the visualization of internalized vesicles that cannot be resolved in standard iSPIM (Fig. 3a). We next applied the m-iSPIM to fixed spheroids (≈500 µm) stained with Vybrant DiO and Alexa Fluor 568-Phalloidin, then loaded in a PDMS microchamber that supports imaging of multiple spheroids. Fig. 3b i) shows stitched brightfield images obtained using the SMF illuminator with three spheroids positioned next to each other within the microchamber. m-iSPIM imaging was then conducted across the highlighted regions as shown in the volumetric reconstruction and 2D cross section in Fig. 3b ii) and iii), respectively. Thus, using the m-iSPIM we can visualize individual cells stained by Vybrant DiO as well as the interstitial space

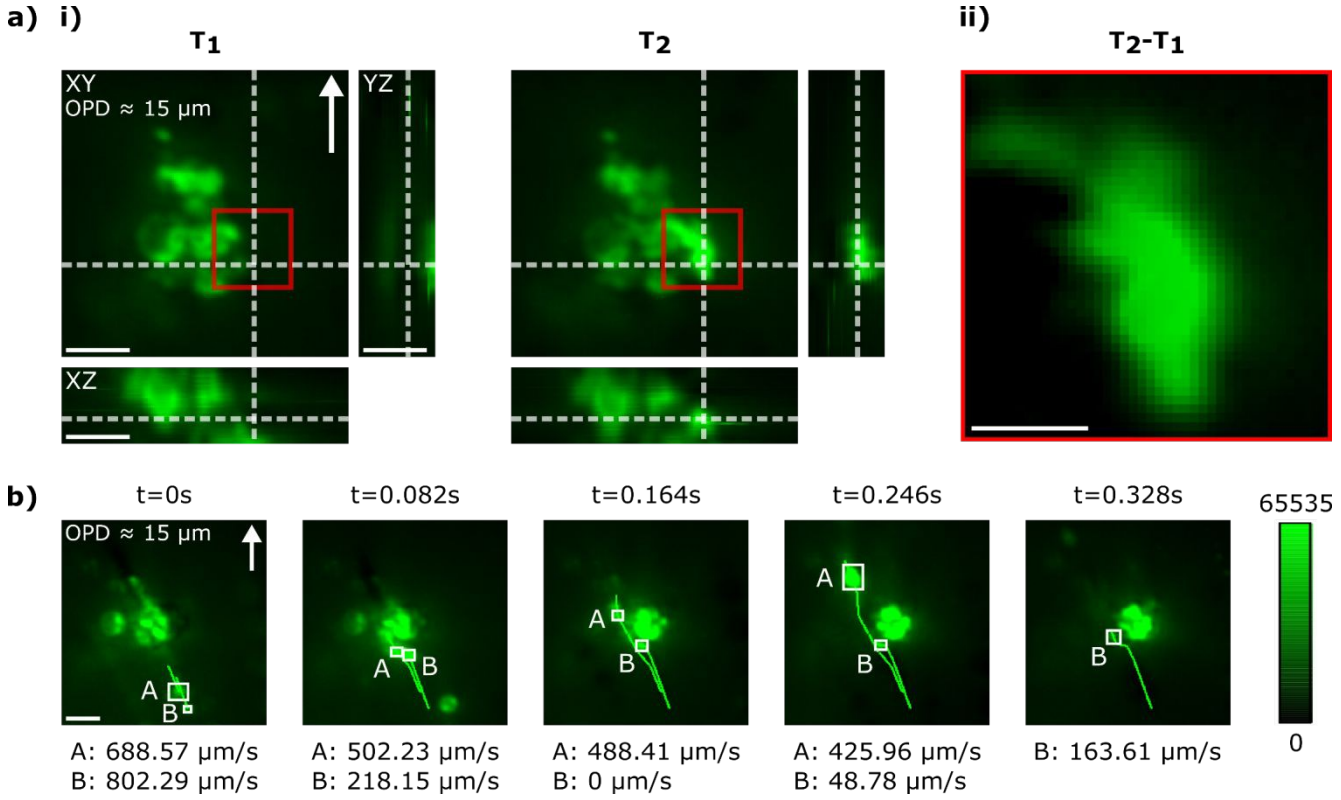

Fig. 4 a) i) Orthogonal views of a $DiOC_6$-labeled platelet aggregate from volumetric scans at two timepoints, T_1 and T_2 with a 15-second interval. Dashed lines indicate a single platelet being recruited into the aggregate. Scale bar: 5 µm. ii) Intensity difference between red box show at time points T_1 and T_2 shown in i) in the red box region Scalebar: 2 µm. b) Tracking of two platelets, indicated as A and B reveal their lateral flow trajectories and velocity near a platelet aggregate. Images are consecutive Z-slices captured during one volumetric scan. Intensity in Fig. 4b) is increased by a factor of two for visualisation purposes. Scale bar: 5 µm. Arrows indicate the flow direction.

View Article Online
DOI: 10.1039/D0LC00598G

between cells marked by the non-specific binding of phalloidin, with an imaging depth penetration of ≈150 μm into the spheroid, owing to the absence of sample optical clearing.[46] The curved microchamber surface visible in Fig. 3b ii) originates from excitation of residual fluorescence dye that is attached to the inner PDMS surface as observed in other studies[47] due to PDMS's hydrophobic property and indicates a d_{media} of ≈50 μm between the microchamber wall and spheroid. These results together demonstrate application of the m-iSPIM in a broad range of biological samples confined within PDMS microdevices.

Next, we carried out a microfluidic platelet aggregate imaging experiment commonly used to evaluate thrombus formation[48] to capture single platelet recruitment into a platelet aggregate using m-iSPIM 3D spatial-temporal imaging capability. Studies of thrombus formation in flowing blood have generally been achieved using confocal microscopy, which is prone to photobleaching.[49, 50] We used the generic intracellular dye $DIOC_6$ to uniformly label washed platelets and then flowed labeled platelets through a 600 μm PDMS circular collage-coated channel at a volume rate of 10 μL/min. In Fig. 4a i), under these modest flow conditions, we observed a platelet aggregate along the margins of the channel outlet at an imaging depth of approximately 150 μm where the lateral imaging resolution is X=0.96±0.04 μm, Y=0.85±0.03 μm. The m-iSPIM collected continuous multiple Z-stack volumes on the platelet aggregate for a total of 5 minutes without signs of photobleaching. From two volumetric scans (15-second interval), we identified a single platelet being recruited into the aggregate indicated by the dashed lines. Since there was minimal movement within the platelet aggregate, we were able to simply subtract the two acquired volumes to identify the spatial location of the recruitment site as shown in Fig. 4a ii). We also attempted to visualize platelet dynamics under flow by conducting image-based tracking. Fig. 4b) shows the trajectories of two platelets flowing pass a platelet aggregate, captured during a single volumetric scan. Here, we calculated platelets' lateral displacements by locating their centroids across multiple Z-slices using intensity thresholding in MATLAB. Platelet velocities were then measured from the spatial-temporal relationship derived from the system's volumetric scan rate.

Discussion

In the current study we have demonstrated the application of tailored PDMS microfluidics for iSPIM, which can be translated to other light sheet microscopy variants such as LLSM,[34] which shares similarities in sample plane geometry.[51] Imaging of living cells/organism in LLSM is compounded by restricted degrees of freedom when loading biological samples and hence, the use of tailored PDMS microfluidics with LLSM or high-NA iSPIM enables controlled sample delivery and in doing so pave the way for high throughput light sheet imaging.[52]

While there are existing specialized multi-immersion objective lenses designed for light sheet imaging of cleared tissues, they have fixed working distances, lower NA (<0.7) and a magnification of around 20X. The implementation of an ETL module to achieve axial focus tuning by controlling the divergence of the excitation beam is applicable to other light sheet objective lenses of different numerical apertures. Moreover, the ETL approach controls the beam divergence precisely without inducing any mechanical movement in the confined sample space, in contrast to piezo-driven methods. An ETL module can also be placed in the detection path[53, 54] to re-focus the imaging plane of the detection objective lenses as required. Hence, the ETL method proposed here would be widely applicable to existing iSPIM or diSPIM setups. However, for a system with high NA detection objective lenses, an additional phase mask may be required to compensate for spherical aberration induced by the ETL module.

Refractive adaptive optics element can also be utilized in the system's excitation and emission paths to conduct wavefront optimization for aberration correction.[55, 56] Unlike light sheet systems customized with reflective AO elements,[57, 58] integrating the transmissive, lens-like AO element requires only simple modification to the system. For detecting wavefront distortions, a wavefront sensorless measurement algorithm can be adopted without modifying the system.[59] We anticipate that this AO implementation not only can compensate for the beam's axial focal shift (a defocus mode) described in our work, but also improve on the current m-iSPIM's limited imaging depth and resolution in densely packed biological samples.

One limitation of the m-iSPIM lies in the imaging setup, which uses an open-top petri dish that is susceptible to evaporation and convection resulting in a non-uniform RI variation across the sucrose solution, albeit at a very slow rate of $\Delta n/sec > 5x10^{-6}$. To avoid this, we have devised a fluidic feedback system (Supplementary Fig. 6) that can maintain a stable sucrose concentration over time. Alternatively, a non-aqueous solution such as silicone oil can circumvent the issue of evaporation but would be less economical than sucrose.

The incorporation of an optical fiber as a light source between the m-iSPIM objective lenses expands the functionality beyond exclusively light sheet fluorescence imaging. While the fiber-based QPM is implemented for $\Delta n_{external}$ quantification, it can be used to perform label-free brightfield or phase imaging on samples.[39] For instance, brightfield imaging (QPM) together with fluorescence imaging in microfluidic-based imaging flow cytometry are important to determine intracellular localization of fluorescent markers.[19, 60-62] For potential adaptive optics implementation, the QPM can serve as a wavefront distortion detection tool based on phase profile directly measured at sample level.[63] However, detection accuracy greatly relies on the knowledge of the refractive index distribution across the sample, which can be difficult to obtain from samples with complex internal geometries. It will also be interesting to determine how photomanipulation techniques including optical tweezers,[64] optogenetics[65] and photoactivation for super resolution microscopy[66] can take advantage of the optical fiber light source, where spatial control is not critical.

Recent development in 3D printing of PDMS device enables direct formation of 3D microchannel structures without micromolding.[67-69] This also provides direct fabrication control

over the device's outer dimension thus ensures good compatibility with the m-iSPIM. However, due to the nature of additive manufacturing, surface roughness as a result of grooves formed between neighboring filaments or layers can lead to undesired scattering and refraction at the internal interface with $\Delta n_{internal}$.[70] Treating the inner PDMS surface with solvent or extra PDMS coating can smoothen the roughness, but with a cost of additional processing.[69] Nevertheless, we believe that PDMS 3D printing approaches will build on top of the conventional soft lithography technique addressed in this work, to serve as a specialized tool for microfluidic application using m-iSPIM.

In addition, PDMS chambers can act as isolated sample holder to image solvent-based clearing agents that are necessary for tissue optical clearing but potentially corrosive to objective lenses[71-73] as well as expansion microscopy where sample can be kept in isolation to ensure tissue hydration.[74] The entire PDMS chamber can then be RI-matched with sucrose solution for cleared tissue imaging.

Finally, this combination of the m-iSPIM and PDMS microdevices can be a powerful multi-modality tool for long-term volumetric imaging in established biological experimental systems in vitro and ex vivo. The ability to perform light sheet imaging on spheroids in microfluidic channels allows wide-ranging imaging of other 3D cellular models under conditions that can recapitulate the physiological environment, and yield cellular responses vastly different from 2D cultures.[75-77] Likewise, containment of biological samples in a PDMS chamber allows for easy manipulation of the cellular microenvironment that is otherwise difficult to achieve in iSPIM and LLSM. More importantly, we demonstrated m-iSPIM's spatial-temporal imaging capability for single platelet dynamic event within a fluidic microenvironment. This will support the application of lightsheet imaging to hemostasis/thrombosis research, that have so far been applied only to fixed sample.[78]

Conclusion

In this work, we demonstrate the feasibility of a light sheet modality called the m-iSPIM that is fully compatible with conventional soft lithography fabricated PDMS microdevice and delivers high-resolution imaging of live cells and fixed spheroids. We proved that the majority of the OPD arises from the RI-mismatch at the external interface of the PDMS microdevice and that this can be easily eliminated by non-hazardous, widely available sucrose solution. The ETL module in the m-iSPIM corrects for any subsequent axial focal shift and so achieves sub-micrometer imaging resolution up to a 200 µm depth within the PDMS microchannel. We anticipate that the m-iSPIM will be a key enabler for a wide range of dynamic high-resolution light sheet microscopy applications for imaging of biological samples that are required to be isolated or delivered in a controlled environment.

Acknowledgements

The authors acknowledge the initial technical assistance and advice from Dr. Xuefei He for QPM and Mr. Thomas McMenamin and Mr. Jon Daniels (ASI) for assistance with the initial set-up of iSPIM. We thank Ms. Samina Nazir and Mr. Marcus Alim for providing washed platelets. We thank David Tscharke for providing L929 fibroblasts and insightful discussion with staff at the Imaging and Cytometry Facility (JCSMR). We are grateful for critical comments of the manuscript from Dr. Hari Shroff and his team at NIH. This work was supported by grants Australian Research Council (DP200100364, DP190100039, DE160100843) and ANU Major Equipment grant (15MEC36, 16MEC26).

Conflicts of interest

There are no conflicts to declare.

References

1 D. Qin, Y. Xia and G. M. Whitesides, *Nature Protocols*, 2010, **5**, 491-502.
2 K. J. Regehr, M. Domenech, J. T. Koepsel, K. C. Carver, S. J. Ellison-Zelski, W. L. Murphy, L. A. Schuler, E. T. Alarid and D. J. Beebe, *Lab on a Chip*, 2009, **9**, 2132-2139.
3 L. K. Chin, C.-H. Lee and B.-C. Chen, *Lab on a Chip*, 2016, **16**, 2014-2024.
4 J. Huisken, J. Swoger, F. Del Bene, J. Wittbrodt and E. H. K. Stelzer, *Science*, 2004, **305**, 1007.
5 P. J. Keller, A. D. Schmidt, J. Wittbrodt and E. H. K. Stelzer, *Science*, 2008, **322**, 1065.
6 J. Huisken and D. Y. R. Stainier, *Development*, 2009, **136**, 1963.
7 F. Pampaloni, U. Berge, A. Marmaras, P. Horvath, R. Kroschewski and E. H. K. Stelzer, *Integrative Biology*, 2014, **6**, 988-998.
8 I. Albert-Smet, A. Marcos-Vidal, J. J. Vaquero, M. Desco, A. Muñoz-Barrutia and J. Ripoll, *Frontiers in Neuroanatomy*, 2019, **13**.
9 A. K. Glaser, N. P. Reder, Y. Chen, C. Yin, L. Wei, S. Kang, L. A. Barner, W. Xie, E. F. McCarty, C. Mao, A. R. Halpern, C. R. Stoltzfus, J. S. Daniels, M. Y. Gerner, P. R. Nicovich, J. C. Vaughan, L. D. True and J. T. C. Liu, *Nature Communications*, 2019, **10**, 2781.
10 X. Chen, S. Hou, J. Chu, Y. Xiong, P. Xiong, G. Liu and Y. Tian, *Micromachines*, 2017, **8**.
11 Y. Wu, A. Ghitani, R. Christensen, A. Santella, Z. Du, G. Rondeau, Z. Bao, D. Colón-Ramos and H. Shroff, *Proceedings of the National Academy of Sciences*, 2011, **108**, 17708.
12 H. Deschout, K. Raemdonck, S. Stremersch, P. Maoddi, G. Mernier, P. Renaud, S. Jiguet, A. Hendrix, M. Bracke, R. Van den Broecke, M. Röding, M. Rudemo, J. Demeester, S. C. De Smedt, F. Strubbe, K. Neyts and K. Braeckmans, *Nanoscale*, 2014, **6**, 1741-1747.
13 B. Patra, Y.-S. Peng, C.-C. Peng, W.-H. Liao, Y.-A. Chen, K.-H. Lin, Y.-C. Tung and C.-H. Lee, *Biomicrofluidics*, 2014, **8**, 052109.
14 R. Galland, G. Grenci, A. Aravind, V. Viasnoff, V. Studer and J.-B. Sibarita, *Nature Methods*, 2015, **12**, 641-644.
15 M. B. M. Meddens, S. Liu, P. S. Finnegan, T. L. Edwards, C. D. James and K. A. Lidke, *Biomed. Opt. Express*, 2016, **7**, 2219-2236.
16 P. Paiè, F. Bragheri, A. Bassi and R. Osellame, *Lab on a Chip*, 2016, **16**, 1556-1560.
17 H. Jiang, T. Zhu, H. Zhang, J. Nie, Z. Guan, C.-M. Ho, S. Liu and P. Fei, *Lab on a Chip*, 2017, **17**, 2193-2197.

18 E. Zagato, T. Brans, S. Verstuyft, D. van Thourhout, J. Missinne, G. van Steenberge, J. Demeester, S. De Smedt, K. Remaut, K. Neyts and K. Braeckmans, *Opt. Express*, 2017, **25**, 1732-1745.
19 T. Miura, H. Mikami, A. Isozaki, T. Ito, Y. Ozeki and K. Goda, *Biomed. Opt. Express*, 2018, **9**, 3424-3433.
20 E. R. Polanco, N. Western and T. A. Zangle, *J Vis Exp*, 2018, DOI: 10.3791/58296, 58296.
21 F. Sala, M. Castriotta, P. Paiè, A. Farina, S. D'Annunzio, A. Zippo, R. Osellame, F. Bragheri and A. Bassi, *Biomed. Opt. Express*, 2020, **11**, 4397-4407.
22 M. B. Bouchard, V. Voleti, C. S. Mendes, C. Lacefield, W. B. Grueber, R. S. Mann, R. M. Bruno and E. M. C. Hillman, *Nature Photonics*, 2015, **9**, 113-119.
23 M. Kumar and Y. Kozorovitskiy, *Opt. Lett.*, 2019, **44**, 1706-1709.
24 V. Voleti, K. B. Patel, W. Li, C. Perez Campos, S. Bharadwaj, H. Yu, C. Ford, M. J. Casper, R. W. Yan, W. Liang, C. Wen, K. D. Kimura, K. L. Targoff and E. M. C. Hillman, *Nature Methods*, 2019, **16**, 1054-1062.
25 R. McGorty, H. Liu, D. Kamiyama, Z. Dong, S. Guo and B. Huang, *Opt. Express*, 2015, **23**, 16142-16153.
26 R. McGorty, D. Xie and B. Huang, *Opt. Express*, 2017, **25**, 17798-17810.
27 L. A. Barner, A. K. Glaser, L. D. True, N. P. Reder and J. T. C. Liu, *Opt. Lett.*, 2019, **44**, 4451-4454.
28 Y. Chen, W. Xie, A. K. Glaser, N. P. Reder, C. Mao, S. M. Dintzis, J. C. Vaughan and J. T. C. Liu, *Biomed. Opt. Express*, 2019, **10**, 1257-1272.
29 A. K. Glaser, K. W. Bishop, L. A. Barner, R. B. Serafin and J. T. C. Liu, *bioRxiv*, 2020, DOI: 10.1101/2020.05.06.081745, 2020.2005.2006.081745.
30 A. Kotnala, Y. Zheng, J. Fu and W. Cheng, *Lab on a Chip*, 2017, **17**, 2125-2134.
31 M. Paturzo, A. Finizio, P. Memmolo, R. Puglisi, D. Balduzzi, A. Galli and P. Ferraro, *Lab on a Chip*, 2012, **12**, 3073-3076.
32 A. Kumar, Y. Wu, R. Christensen, P. Chandris, W. Gandler, E. McCreedy, A. Bokinsky, D. A. Colón-Ramos, Z. Bao, M. McAuliffe, G. Rondeau and H. Shroff, *Nature Protocols*, 2014, **9**, 2555-2573.
33 Y. Wu, A. Kumar, C. Smith, E. Ardiel, P. Chandris, R. Christensen, I. Rey-Suarez, M. Guo, H. D. Vishwasrao, J. Chen, J. Tang, A. Upadhyaya, P. J. La Riviere and H. Shroff, *Nature Communications*, 2017, **8**, 1452.
34 B.-C. Chen, W. R. Legant, K. Wang, L. Shao, D. E. Milkie, M. W. Davidson, C. Janetopoulos, X. S. Wu, J. A. Hammer, Z. Liu, B. P. English, Y. Mimori-Kiyosue, D. P. Romero, A. T. Ritter, J. Lippincott-Schwartz, L. Fritz-Laylin, R. D. Mullins, D. M. Mitchell, J. N. Bembenek, A.-C. Reymann, R. Böhme, S. W. Grill, J. T. Wang, G. Seydoux, U. S. Tulu, D. P. Kiehart and E. Betzig, *Science*, 2014, **346**, 1257998.
35 W. F. Quirós-Solano, N. Gaio, O. M. J. A. Stassen, Y. B. Arik, C. Silvestri, N. C. A. Van Engeland, A. Van der Meer, R. Passier, C. M. Sahlgren, C. V. C. Bouten, A. van den Berg, R. Dekker and P. M. Sarro, *Scientific Reports*, 2018, **8**, 13524.
36 F. Pampaloni, N. Ansari and E. H. K. Stelzer, *Cell and Tissue Research*, 2013, **352**, 161-177.
37 R. Sandmann and S. Köster, *Scientific Reports*, 2016, **6**, 22357.
38 A. D. Edelstein, M. A. Tsuchida, N. Amodaj, H. Pinkard, R. D. Vale and N. Stuurman, *Journal of Biological Methods; Vol 1, No 2 (2014)*, 2014.
39 E. Cuche, P. Marquet and C. Depeursinge, *Appl. Opt.*, 2000, **39**, 4070-4075.
40 A. Barty, K. A. Nugent, D. Paganin and A. Roberts, *Opt. Lett.*, 1998, **23**, 817-819.
41 B. F. Grewe, F. F. Voigt, M. van 't Hoff and F. Helmchen, *Biomed. Opt. Express*, 2011, **2**, 2035-2046.
42 J. Schindelin, I. Arganda-Carreras, E. Frise, V. Kaynig, M. Longair, T. Pietzsch, S. Preibisch, C. Rueden, S. Saalfeld, B. Schmid, J.-Y. Tinevez, D. J. White, V. Hartenstein, K. Eliceiri, P. Tomancak and A. Cardona, *Nature Methods*, 2012, **9**, 676-682.
43 K. Becker, S. Saghafi, M. Pende, I. Sabdyusheva-Litschauer, C. M. Hahn, M. Foroughipour, N. Jährling and H.-U. Dodt, *Scientific Reports*, 2019, **9**, 17625.
44 A. S. Cruz-Félix, A. Santiago-Alvarado, J. Márquez-García and J. González-García, *Heliyon*, 2019, **5**, e03064.
45 E. Remacha, L. Friedrich, J. Vermot and F. O. Fahrbach, *Biomed. Opt. Express*, 2020, **11**, 8-26.
46 J. F. Dekkers, M. Alieva, L. M. Wellens, H. C. R. Ariese, P. R. Jamieson, A. M. Vonk, G. D. Amatngalim, H. Hu, K. C. Oost, H. J. G. Snippert, J. M. Beekman, E. J. Wehrens, J. E. Visvader, H. Clevers and A. C. Rios, *Nature Protocols*, 2019, **14**, 1756-1771.
47 K. H. K. Wong, J. F. Edd, S. N. Tessier, W. D. Moyo, B. R. Mutlu, L. D. Bookstaver, K. L. Miller, S. Herrara, S. L. Stott and M. Toner, *Lab on a Chip*, 2018, **18**, 2146-2155.
48 X. He, S. J. Montague, X. Tao, E. E. Gardiner and W. M. Lee, *Advanced Biosystems*, 2018, **2**, 1800089.
49 O. Agbani Ejaife, T. J. van den Bosch Marion, E. Brown, M. Williams Christopher, J. A. Mattheij Nadine, M. E. M. Cosemans Judith, W. Collins Peter, W. M. Heemskerk Johan, I. Hers and W. Poole Alastair, *Circulation*, 2015, **132**, 1414-1424.
50 S. M. de Witt, F. Swieringa, R. Cavill, M. M. E. Lamers, R. van Kruchten, T. Mastenbroek, C. Baaten, S. Coort, N. Pugh, A. Schulz, I. Scharrer, K. Jurk, B. Zieger, K. J. Clemetson, R. W. Farndale, J. W. M. Heemskerk and J. M. E. M. Cosemans, *Nature Communications*, 2014, **5**, 4257.
51 C. T. Russell and E. J. Rees, *bioRxiv*, 2019, DOI: 10.1101/636977, 636977.
52 C.-Y. Chen, Y.-T. Liu, C.-H. Lu, P.-Y. Lee, Y.-C. Tsai, J.-S. Wu, P. Chen and B.-C. Chen, *Micromachines*, 2019, **10**.
53 F. O. Fahrbach, F. F. Voigt, B. Schmid, F. Helmchen and J. Huisken, *Opt. Express*, 2013, **21**, 21010-21026.
54 M. Duocastella, G. Sancataldo, P. Saggau, P. Ramoino, P. Bianchini and A. Diaspro, *ACS Photonics*, 2017, **4**, 1797-1804.
55 S. Bonora, Y. Jian, P. Zhang, A. Zam, E. N. Pugh, R. J. Zawadzki and M. V. Sarunic, *Opt. Express*, 2015, **23**, 21931-21941.
56 P. Pozzi, M. Quintavalla, A. Wong, J. Borst, S. Bonora and M. Verhaegen, *Opt. Lett.*, 2020, **45**, 3585-3588.
57 C. Bourgenot, C. D. Saunter, J. M. Taylor, J. M. Girkin and G. D. Love, *Opt. Express*, 2012, **20**, 13252-13261.
58 R. Jorand, G. Le Corre, J. Andilla, A. Maandhui, C. Frongia, V. Lobjois, B. Ducommun and C. Lorenzo, *PLOS ONE*, 2012, **7**, e35795.
59 M. J. Booth, *Opt. Express*, 2006, **14**, 1339-1352.
60 R. regmi, K. Mohan and P. P. Mondal, *Microscopy Research and Technique*, 2013, **76**, 1101-1107.
61 R. Regmi, K. Mohan and P. P. Mondal, *AIP Advances*, 2014, **4**, 097125.
62 C. K. Rasmi, S. Padmanabhan, K. Shirlekar, K. Rajan, R. Manjithaya, V. Singh and P. P. Mondal, *Applied Physics Letters*, 2017, **111**, 243702.
63 H. Lück, K. O. Müller, P. Aufmuth and K. Danzmann, *Optics Communications*, 2000, **175**, 275-287.
64 C. Liberale, G. Cojoc, F. Bragheri, P. Minzioni, G. Perozziello, R. La Rocca, L. Ferrara, V. Rajamanickam, E. Di Fabrizio and I. Cristiani, *Scientific Reports*, 2013, **3**, 1258.
65 P. Kaur, T. E. Saunders and N. S. Tolwinski, *Scientific Reports*, 2017, **7**, 16636.
66 A.-K. Gustavsson, P. N. Petrov and W. E. Moerner, *Opt. Express*, 2018, **26**, 13122-13147.
67 T. J. Hinton, A. Hudson, K. Pusch, A. Lee and A. W. Feinberg, *ACS Biomaterials Science & Engineering*, 2016, **2**, 1781-1786.
68 V. Ozbolat, M. Dey, B. Ayan, A. Povilianskas, M. C. Demirel and I. T. Ozbolat, *ACS Biomaterials Science & Engineering*, 2018, **4**, 682-693.
69 M. Riahi, F. Karimi and A. Ghaffari, *Rapid Prototyping Journal*, 2019, **25**, 775-780.

View Article Online
DOI: 10.1039/D0LC00598C

70 P. J. Nuñez, A. Rivas, E. García-Plaza, E. Beamud and A. Sanz-Lobera, *Procedia Engineering*, 2015, **132**, 856-863.
71 S. M. Grist, S. S. Nasseri, T. Poon, C. Roskelley and K. C. Cheung, *Biomicrofluidics*, 2016, **10**, 044107.
72 T. Chakraborty, M. K. Driscoll, E. Jeffery, M. M. Murphy, P. Roudot, B.-J. Chang, S. Vora, W. M. Wong, C. D. Nielson, H. Zhang, V. Zhemkov, C. Hiremath, E. D. De La Cruz, Y. Yi, I. Bezprozvanny, H. Zhao, R. Tomer, R. Heintzmann, J. P. Meeks, D. K. Marciano, S. J. Morrison, G. Danuser, K. M. Dean and R. Fiolka, *Nature Methods*, 2019, **16**, 1109-1113.
73 A. P. Di Giovanna, C. Credi, A. Franceschini, M. C. Müllenbroich, L. Silvestri and F. S. Pavone, *Frontiers in Neuroanatomy*, 2019, **13**.
74 C. Zhang, J. S. Kang, S. M. Asano, R. Gao and E. S. Boyden, *Current Protocols in Neuroscience*, 2020, **92**, e96.
75 C. McKee and G. R. Chaudhry, *Colloids and Surfaces B: Biointerfaces*, 2017, **159**, 62-77.
76 O. V. Au - Halaidych, F. Au - van den Hil, C. L. Au - Mummery and V. V. Au - Orlova, *JoVE*, 2018, DOI: doi:10.3791/58678, e58678.
77 E. Leary, C. Rhee, B. T. Wilks and J. R. Morgan, *SLAS TECHNOLOGY: Translating Life Sciences Innovation*, 2018, **23**, 231-242.
78 N. E. Buglak, J. Lucitti, P. Ariel, S. Maiocchi, F. J. Miller, Jr. and E. S. M. Bahnson, *Cardiovascular Research*, 2020, DOI: 10.1093/cvr/cvaa037.